CHAPTER 2
SIMPLY-SUPPORTED CYLINDER STRUCTURAL RESPONSE

In this chapter the structural response of a simply-supported (SS) cylinder excited by piezoelectric (PZT) actuators is addressed. Initially the theoretical formulation of Lalande's impedance model of a PZT actuator exciting a SS cylinder is reviewed. The creation of a SS boundary condition on an actual cylinder is also described. The experimental results for the created cylinder are then presented and compared to the impedance model and finite element analysis results. The goal of the work presented here is to verify the analytical model of a SS cylinder excited by PZT actuators. Once the model is validated, it can be used to predict the structural response of a large scale cylinder which emulates a rocket payload fairing (PF).

2.1 PZT Actuator Model and Structural Response for a SS Cylinder

In this dissertation the structural response of a SS cylinder excited by PZT actuators is determined using the model developed by Lalande. This model was chosen because it incorporates the effects caused by the curvature of the actuators and the changing structural impedance of the cylinder as a function of frequency. Not considering the changing impedance of the structure can lead to an incorrect predicted response (Lalande, 1995). Other models are discussed in section 1.7. A brief overview of this model will now be presented.

The coordinate system used for the cylinder and actuator is shown in Fig. 2.1. The model assumes two rectangular PZT actuators are attached to the cylinder, one on the outer surface and another collocated on the inner surface. The resultant forces (in phase actuation) and moments (out of phase actuation) are assumed to act at the cylinder's midplane as shown in Fig. 2.2.

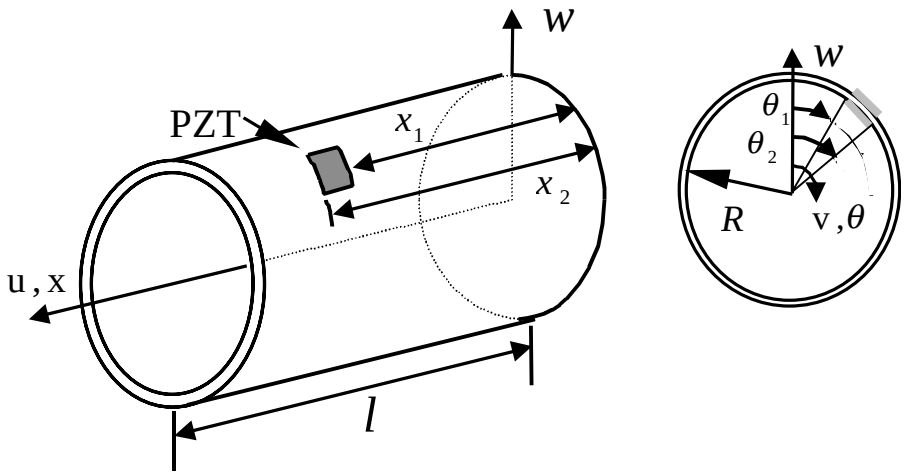

Figure 2.1 Cylinder with mounted actuators.

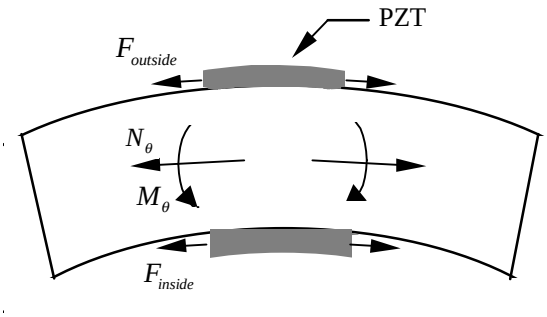

Figure 2.2 Transfer of actuator forces to equivalent mid-plane loading.

The relationship between the actuator output force and the equivalent midplane force or moment in the axial or tangential direction is given by:

inphase:

$$N_x = 2F_x \tag{2.1a}$$

$$N_\theta = 2F_\theta \tag{2.1b}$$

out of phase:

$$M_x = (t_a + t_s)F_x \tag{2.1c}$$

$$M_\theta = (t_a + t_s)F_\theta \tag{2.1d}$$

where t_a and t_s are the actuator and shell thickness, respectively. The actuator forces F_x and F_θ need to be solved by using the PZT actuator constitutive equations, actuator impedance and the structural impedance or admittance (see Fig. 2.3). The structural impedance along the actuator edge is related to the structural admittance by:

$$\begin{bmatrix} Z_{xx} & Z_{x\theta} \\ Z_{\theta x} & Z_{\theta\theta} \end{bmatrix} = \begin{bmatrix} H_{xx} & H_{x\theta} \\ H_{\theta x} & H_{\theta\theta} \end{bmatrix}^{-1} \tag{2.2}$$

where Z and H represent the structural impedance and admittance, respectively. The structural admittance will be discussed later. The input impedance (shorted) of the PZT actuators are given by:

direct terms:

$$Z_{axx} = \frac{Y_a^E t_a \kappa R_a}{i\omega \tan(\kappa l_a)} \tag{2.3a}$$

$$Z_{a\theta\theta} = \frac{Y_a^E t_a \kappa l_a}{i\omega \tan(\kappa R_a)} \tag{2.3b}$$

cross terms:

$$Z_{ax\theta} = \frac{Y_a^E t_a \kappa l_a}{i\omega \tan(\kappa l_a)} \tag{2.3c}$$

$$Z_{a\theta x} = \frac{Y_a^E t_a \kappa R_a}{i\omega \tan(\kappa R_a)} \tag{2.3d}$$

where, Y_a^E is the actuator complex modulus of elasticity with no applied electric field, R_a is the actuator angular length, l_a is the actuator axial length, ω represents the angular frequency, i is an imaginary number, and κ is given by:

$$\kappa = \omega \sqrt{\rho_a / Y_a^E} \tag{2.4}$$

where, ρ_a is the density of the actuator.

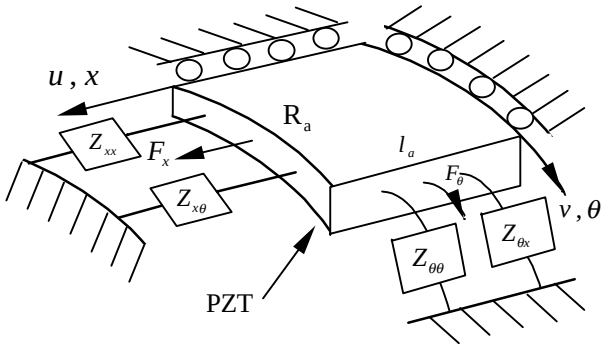

Figure 2.3 Interaction between the PZT and the cylinder via the structural impedance.

Combining the actuator impedances, Eq. 2.3, with the PZT constitutive equations and applying boundary conditions, a relationship between the dynamic actuator force and the structural impedance (Eq. 2.2) results (Zhou et al., 1993, Lalande, 1995):

$$F_x = \frac{-i\omega}{R_a}\left(A\sin(\kappa l_a)Z_{xx} + C\sin(\kappa R_a)Z_{x\theta}\right)e^{i\omega t} \tag{2.5a}$$

$$F_\theta = \frac{-i\omega}{l_a}\left(A\sin(\kappa l_a)Z_{\theta x} + C\sin(\kappa R_a)Z_{\theta\theta}\right)e^{i\omega t} \tag{2.5b}$$

where, A and C are calculated from,

$$\begin{Bmatrix} A \\ C \end{Bmatrix} = \begin{bmatrix} \kappa\cos(\kappa l_a)\left(1 - \nu_a \frac{Z_{x\theta}}{Z_{ax\theta}} + \frac{Z_{xx}}{Z_{axx}}\right) & \kappa\cos(\kappa R_a)\left(\frac{Z_{\theta x}}{Z_{a\theta x}} - \nu_a \frac{Z_{\theta\theta}}{Z_{a\theta\theta}}\right) \\ \kappa\cos(\kappa l_a)\left(\frac{Z_{x\theta}}{Z_{ax\theta}} - \nu_a \frac{Z_{xx}}{Z_{axx}}\right) & \kappa\cos(\kappa R_a)\left(1 - \nu_a \frac{Z_{\theta x}}{Z_{a\theta x}} + \frac{Z_{\theta\theta}}{Z_{a\theta\theta}}\right) \end{bmatrix}^{-1} \begin{Bmatrix} d_{31} \\ d_{32} \end{Bmatrix} E_f \tag{2.6}$$

where, ν_a, d_{31} and d_{32} are the actuator Poisson ratio and PZT constants and E_f is the applied electric field. By using Eqs. 2.1 and 2.5, the actuator output forces and moments can be used to

determine the structural response assuming the structural impedance is known. The computation of the structural response and structural impedance shall be presented next.

To determine the structural response of the SS cylinder caused by the actuation of the PZT actuator, a modal expansion analysis is performed. The equations that describe the motion of the cylinder are based on Love's equations for shell structures. The general equations have been adapted to incorporate loading caused by the actuation of line moments or forces (Soedel, 1981). Subsequently, the equations are developed to incorporate the loading generated by PZT actuators (Zhou et al., 1993, Lalande et al., 1995).

For a cylinder, the natural orthogonal modes can be used to determine the forced response using an infinite series:

$$u_i(x,\theta,t) = \sum_{k=1}^{\infty} p_k(t) U_{ik}(x,\theta) e^{i\omega t} \tag{2.7}$$

where, the subscript i corresponds to the associated displacement (i.e. $i = 3$ represents transverse displacement), $p_k(t)$ represents the modal participation factor and $U_{ik}(x,\theta)$ is the spatial mode shape. For a SS cylinder the mode shape is given by (Soedel, 1981):

$$U_{1k}(x,\theta) = A_{mnp} \cos(\alpha x)\cos(n\theta) \tag{2.8a}$$

$$U_{2k}(x,\theta) = B_{mnp} \sin(\alpha x)\sin(n\theta) \tag{2.8b}$$

$$U_{3k}(x,\theta) = C_{mnp} \sin(\alpha x)\cos(n\theta) \tag{2.8c}$$

$$\alpha = \frac{m\pi}{l} \tag{2.8d}$$

where subscripts m and n represent the modal indices and subscript p refers to one of the three principal coordinates (1,2,3). After performing the standard modal expansion procedure to the differential equations (multiplying by the mode shape, integrating over the domain, and applying orthogonality conditions), the modal participation factor can be determined by solving an ordinary differential equation with a redefined forcing function:

$$\ddot{p}_k(t) + \omega_k^2 p_k(t) = F_k e^{i\omega t} \tag{2.9}$$

where, F_k is the a modified forcing function determined by the actuator forcing terms in the differential equation. The modified forcing function is defined in other references and not included here for brevity (Soedel, 1981). The solution to the modal participation factor can be given in the form:

$$p_k = \frac{F_k}{\omega_k^2 - \omega^2} \tag{2.10}$$

Note that an equivalent damping factor has not been included in this formulation but instead shall be included as a structural damping term with the modulus of elasticity. Equations 2.8 and 2.10 are then substituted into Eq. 2.7 to obtain the response of the cylinder. This analysis was performed by Lalande and the result leads to the structural response of the cylinder (Lalande et al., 1995, Lalande, 1995):

$$w(x,\theta,t)=\sum_{p=1}^{3}\sum_{m=1}^{\infty}\sum_{n=1}^{\infty}\left[\vartheta(S_\theta\cos n\theta-C_\theta\sin n\theta)C_x\sin\alpha x\right]e^{i\omega t} \tag{2.11}$$

where,

$$\vartheta=\frac{R}{\rho_s t_s N^*_{mnp}(\omega^2_{mnp}-\omega^2)}\left[-\frac{A_{mnp}}{C_{mnp}}\left(\frac{N_x}{n}\right)+\frac{B_{mnp}}{C_{mnp}}\left(\frac{N_\theta}{R\alpha}+\frac{M_\theta}{R^2\alpha}\right)+\left(\frac{N_\theta}{R\alpha n}+\frac{M_x\alpha}{n}+\frac{M_\theta n}{R^2\alpha}\right)\right.$$

$$S_\theta=\sin n\theta_1-\sin n\theta_2$$
$$C_\theta=\cos n\theta_1-\cos n\theta_2$$
$$C_x=\cos\alpha x_1-\cos\alpha x_2$$

where, N^*_{mnp} is the mode normalization constant:
inphase:

$$N^*_{mnp}=\frac{Rl\pi}{2}\left(\frac{A_{mnp}}{C_{mnp}}^2+\frac{B_{mnp}}{C_{mnp}}^2+1\right)\quad n\neq 0,\quad m\neq 0$$

out of phase:

$$N^*_{mnp}=\frac{Rl\pi}{2}\left(\frac{B_{mnp}}{C_{mnp}}^2+1\right)\quad n\neq 0,\quad m\neq 0$$

The ratios A_{mnp}/C_{mnp} and B_{mnp}/C_{mnp} can be found in work by Soedel (Soedel, 1981). Finally the structural impedance needs to be described. For two dimensional structures, the admittance matrix is given by (Lalande, 1995):

$$\left(2\dot{u}\Big|_{inphase}-\varsigma\frac{\partial\dot{w}}{\partial x}\Big|_{outphase}\right)\Bigg|_{x=x_2}-\left(2\dot{u}\Big|_{inphase}-\varsigma\frac{\partial\dot{w}}{\partial x}\Big|_{outphase}\right)\Bigg|_{x=x_1}=-(H_{xx}F_x+H_{\theta x}F_\theta) \tag{2.12a}$$

$$\left(2\dot{v}\Big|_{inphase}-\varsigma\frac{\partial\dot{w}}{R\partial\theta}\Big|_{outphase}\right)\Bigg|_{\theta=\theta_2}-\left(2\dot{v}\Big|_{inphase}-\varsigma\frac{\partial\dot{w}}{R\partial\theta}\Big|_{outphase}\right)\Bigg|_{\theta=\theta_1}=-(H_{x\theta}F_x+H_{\theta\theta}F_\theta) \tag{2.12b}$$

where,

$$\varsigma=\frac{(t_s+t_a)^2}{2}$$

Based on the structural admittance defined in Eq. 2.12, the direct structural admittances are determined by dividing the axial or angular velocity by the appropriate force, F_x or F_θ. For brevity, only H_{xx} is presented. The remainder of the admittances can be found in prior citations (Lalande et al., 1995, Lalande, 1995).

$$H_{xx}=\frac{1}{R(\theta_2-\theta_1)}\sum_{p=1}^{3}\sum_{m=1}^{\infty}\sum_{n=1}^{\infty}\left\{\left(\frac{\chi_{in}}{n}\left(\frac{A_{mnp}}{C_{mnp}}\right)^2+\frac{\chi_{out}\alpha^2}{n}\right)(S_\theta\cos n\theta_o-C_\theta\sin n\theta_o)C_x\right\} \tag{2.13}$$

where,

$$\chi_{in} = -\frac{Ri\omega}{\rho_s t_s} \frac{2C_x}{N^*_{mnp}(\omega^2_{mnp} - \omega^2)}$$

$$\chi_{out} = -\frac{Ri\omega}{\rho_s t_s} \frac{(t_s + t_a)^2}{2N^*_{mnp}(\omega^2_{mnp} - \omega^2)} C_x$$

where θ_o refers to the actuator center. The structural admittance (Eq. 2.13) can now be used with Eq. 2.2 to determine the structural impedance, and therefore the actuator forces can be determined and substituted into Eq. 2.11 to determine the transverse displacement of the cylinder. It is the transverse velocity component of the cylinder that generates the acoustic field, and is what is of interest in this work.

2.2 Creation of the Cylinder Simply-Supported Boundary Condition

Many aerospace and structural dynamics problems are too difficult to model analytically with exacting detail. To determine the general behavior of a distributed parameter system, researchers approximate complicated structures with simpler models such as beams, plates and cylinders. Idealized cylinders are used to approximate more complex structures such as airplane fuselages and rocket payload fairings (Niezrecki and Cudney, 1997, Lester and Lefebvre, 1991, Bullmore et al., 1987). Previously, Arnold and Warburton performed some experiments on small diameter cylinders (97.8 mm diameter). They created a SS boundary condition by accurately machining a steel plate to fit the bore of the cylinder. The end-condition tolerance was found to be extremely critical in obtaining results that are in fair agreement with the theory (Arnold and Warburton, 1949). Sewall compared experiments on SS cylindrically curved panels with analysis. But no experiments on cylinders were performed (Sewall, 1967). Koga also studied the effects of boundary conditions on the free vibration of circular cylindrical shells. However, none of the boundary conditions he tested can be considered simply-supported (Koga, 1988). Presented in this section are the steps taken in creating a physical boundary condition which approximates the ideal boundary condition for a SS cylinder. A variety of physical boundary conditions are tested and compared to determine the supports that most closely resemble the ideal SS boundary condition. The experimental results are compared to finite element analysis FEA (using the software package I-DEAS) and to the analytical prediction based on Love's shell theory.

2.2.1 Various Boundary Conditions Tested

The overall experimental setup used to model a SS cylinder is shown in Fig. 2.4. The structure consists of an aluminum cylinder with several collocated PZT actuators (G1195) attached at three different positions A, B, and C, driven in phase (A: $x = 0.2032$ m, $\theta = 0^\circ$; B: $x = 0.1355$ m, $\theta = 0^\circ$; C: $x = .3048$ m, $\theta = 22.5^\circ$). The boundary conditions are created by using two thin aluminum annular shims (0.254 m outer diameter) and two or four aluminum endplates (0.2223 m diameter). The shims are screwed to the cylinder ends and bolted to the endplates (see Fig. 2.5). Resin-dam vacuum sealant is used as a viscoelastic damping material when specified. The physical properties of the instrumented cylinder are described in Table 2.1. The purpose of the annular shim is to prevent the transverse motion of the cylinder at its two ends. This should be attainable since the membrane (in-plane) stiffness of the shim is very large. The shim is also

kept thin so the bending moment introduced by the shim at the cylinder edges is very small. Since the bending stiffness is proportional to the cube of the thickness, for a plate, the stiffness of the cylinder should be several orders of magnitude larger than that of the shim. Likewise for the endplate, compared to the shim. To create a test stand that approximates a SS boundary condition, five different physical configurations were tested.

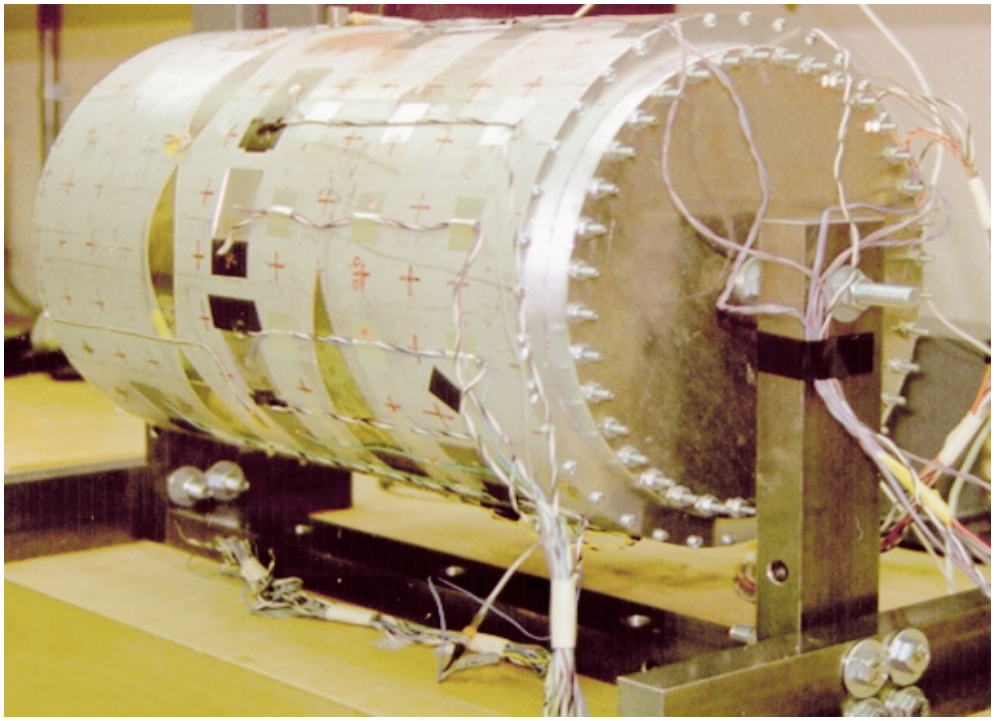

Figure 2.4 Instrumented cylinder.

Table 2.1 Cylinder and actuator properties

Property	Cylinder	PZT Actuator
Young's Modulus (Pa)	$64x10^9$	$63x10^9$
Density (Kg/m^3)	2700	7600
Poisson's Ratio	0.3	0.3
Loss Factor	0.005	0.001
Length (mm)	406.4	38.1
Diameter (mm)	254	-
Thickness (mm)	6.35	0.2413
Width (mm)	-	31.5
Applied Voltage	-	50 or 25 Vrms
d_{32} (m/V)	-	$-166x10^{-12}$

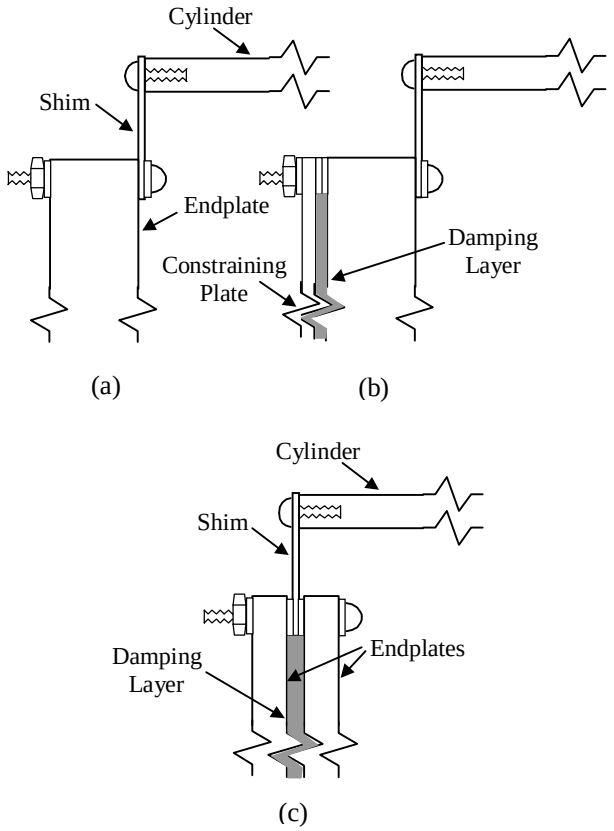

Figure 2.5 Tested boundary conditions: (a) test 1, 2, & 3: (b) test 4: (c) test 5.

Test 1: For the first test, the annular shim (0.508 mm thick) is screwed to the ends of the cylinder and is attached to a 12.7 mm thick circular endplate (Figure 2.5a).

Test 2: The setup is identical to Test 1 except a thinner annular shim (0.4064 mm) is used. This change was performed to see how altering the thickness (stiffness) of the shim affected the response.

Test 3: The setup is identical to Test 2 except the annular shim is now discontinuous and consists of 18 individual radially sliced, slotted segments. Each of the individual segments contains a radial slot 9.525 mm deep (0.762 mm wide) on the outer and inner edge located at the middle of the segment. This change was performed to reduce the coupling between the endplates and the cylinder.

Test 4: The setup is identical to Test 1 except a layer of damping material (2.08 mm) has been added along with a circular constraining aluminum plate (0.2223 m diameter, 1.588 mm thick). The plate is bolted outside of the cylinder onto the endplates. This change was designed to introduce some damping into the endplates and reduce their vibration (Figure 2.5b).

Test 5: The final setup used the same annular shim as in Test 1 except it is now being sandwiched in the middle between two 6.35 mm thick aluminum endplates (four in all). A layer

of damping material (2.59 mm) separates the plates. This change was designed to center the shim at the neutral axis of the endplate and so the high in-plane forces in the annular shim can not excite the transverse displacement of the endplates. This change also placed the damping material in a region of maximum shear. The goal is to reduce the coupling between the endplates and the cylinder (Fig 2.5c).

2.2.2 Synopsis of Boundary Conditions Tested

The displacement of the cylinder at $x = 0.1016\,\text{m}$, $q = 0^\circ$ (actuated by actuator B, 50 Vrms) for the five different boundary conditions can be seen in Fig. 2.6. The circled region indicates where the largest interaction between the endplates and the cylinder occurs. This region corresponds to the second natural frequency of the circular endplate. The thinner shim from Test 2 is more strongly coupled than the 0.508 mm shim from Test 1. It was expected that the slotted shim in Test 3 would decouple the endplate from the cylinder, however this was not found to be true. The effect of the slots was also found to increase the displacement at the ends of the cylinder. The fourth test implemented a constrained damping layer as shown in Figure 2.5b. The damping layer did reduce endplate/cylinder interaction. The final test placed the shim at the neutral axis of the endplate and is denoted by the darkest of the five lines in Fig. 2.6. Test five shows very little coupling between the cylinder and the endplate. Although not shown, Test 5 also resulted in the smallest edge displacements by far and an order of magnitude decrease in the vibration of the endplates for virtually all frequencies compared to any of the other tests. The remaining experiments are performed using the boundary conditions described for Test 5 (Fig 2.5c).

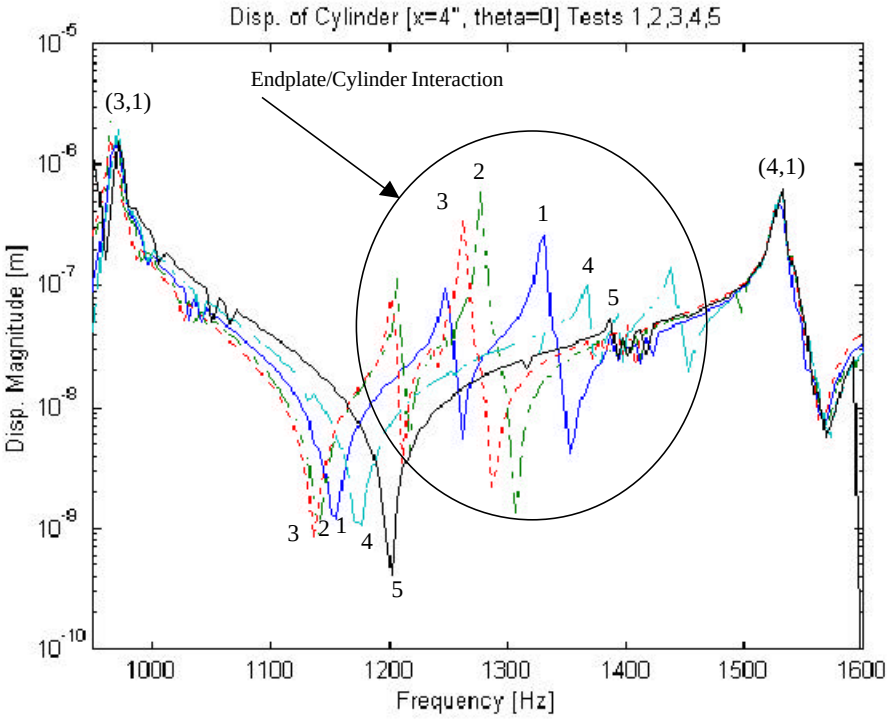

Figure 2.6 Response of the cylinder for different boundary conditions (tests 1-5).

2.3 Modal Evaluation of the Cylinder

To determine the modal properties of the cylinder a roving modal hammer test was performed. A Kistler 8620 accelerometer was used to measure the response (at $x = 0.359$ m, $q = 0^{\circ}$) for various equally spaced axial ($x = 0$, 33.87, 67.73, 101.6,...372.5, 406.4 mm., $q = 0^{\circ}$) and angular ($x =$ 67.73 and 237.1 mm, $q = 0, 10, 20, \ldots, 180^{\circ}$) impact positions using a Kistler 9712A50 force transducer. Because of the reciprocity principle, the hammer was moved instead of the accelerometer. This produces equivalent results to a roving accelerometer test.

The FRF's for half of the cylinder in the axial direction are shown in Fig. 2.7 (hammer strikes at $x = 0$, 33.87, 67.73, 101.6, 135.5, 169.3, 203.2 mm, $q = 0^{\circ}$). The corresponding phase information can be found in Appendix H. Little can be learned from Fig. 2.7 except for the location of the resonant frequencies. The modal indices (n, m: circumferential, axial) are placed next to the associated peak for clarity. To determine the dominant modal index at a particular frequency it is necessary to look at Figs. 2.8-2.10. The axial modal index is determined from Fig. 2.8 by observing the spatial displacement pattern at a particular frequency. It should be noticed that the displacements at the edges of the cylinder are very small compared to the displacement away from the edge. This is what is expected for a cylinder with SS boundary conditions. The circumferential modal index is determined by observing the displacement pattern for various angular positions at a given frequency. Since measurements were performed only on half of the cylinder, the results in the angular direction are mirrored about $q = 180^{\circ}$. Results are shown for only two frequencies, 950 Hz and 1838 Hz, due to space limitations (see Figs. 2.9 and 2.10). From Figs. 2.9 it is determined that the resonant frequency at 950 Hz corresponds to the (2,1) mode for the cylinder. Likewise, the resonant frequency at 1838 Hz corresponds to the (3,2) mode for the cylinder (see Fig 2.10).

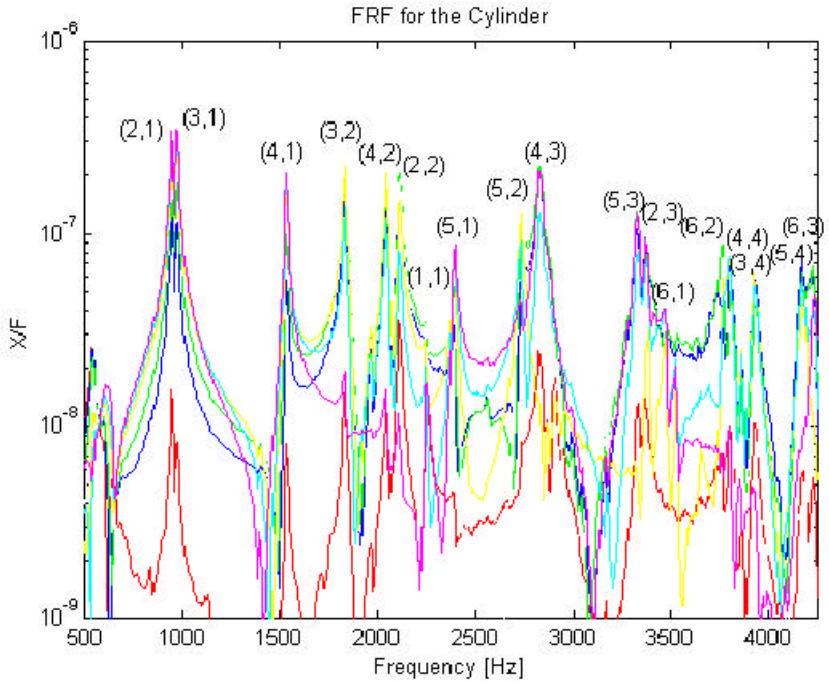

Figure 2.7 Response of the cylinder at different axial locations.

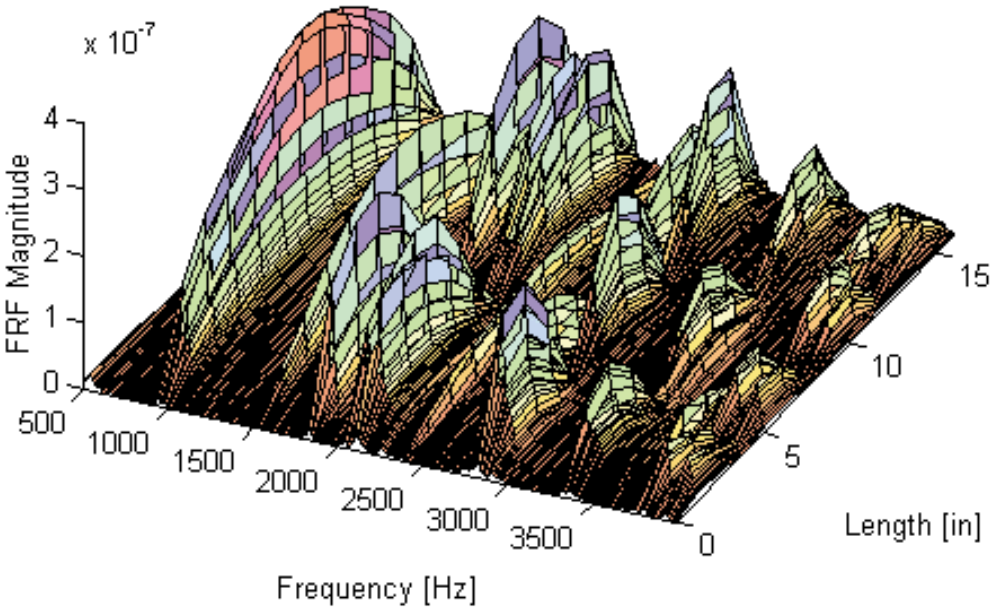

Figure 2.8 FRF of accelerance with respect to force.

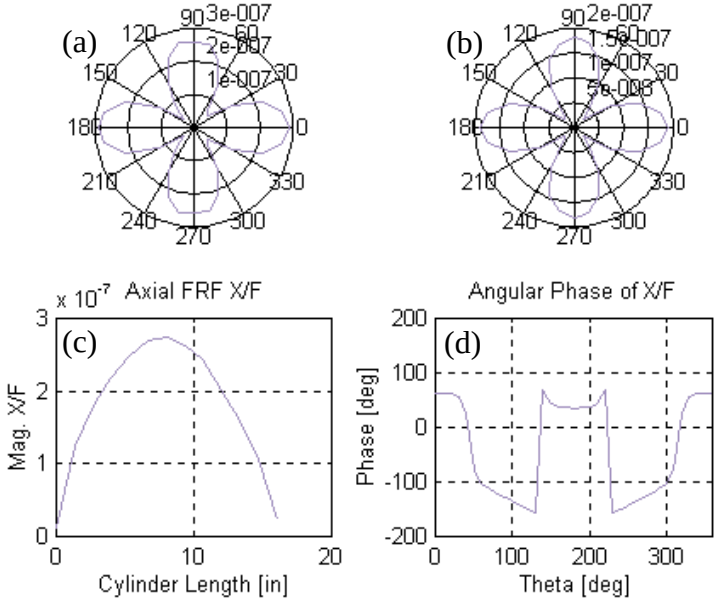

Figure 2.9. Spatial FRF magnitude at 950 Hz (2,1): (a) circumferential at x = 237 mm: (b) circumferential at x = 67.8 mm: (c) axial at $\theta = 0^{\circ}$: (d) circumferential phase at x = 67.8 mm.

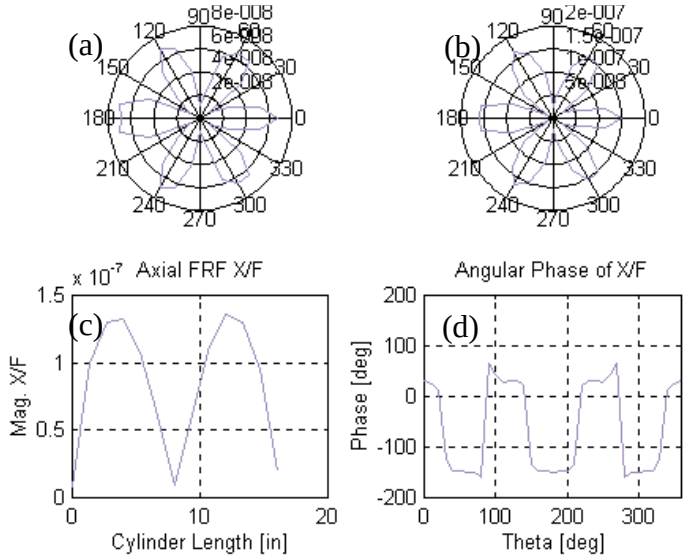

Figure 2.10 Spatial FRF at 1838 Hz (3,2): (a) circumferential at x = 237 mm: (b) circumferential at x = 67.8 mm: (c) axial at $\theta = 0^{\circ}$: (d) circumferential phase at x = 67.8 mm.

2.4 Comparison with Finite Element Analysis

A finite element analysis (FEA) was also performed to compare with the natural frequencies obtained analytically and experimentally for the cylinder. A finite element model was created with the software I-DEAS using 30 axial and 72 circumferential thin shell elements. The FEA model does not include any stiffening elements around the edge of the cylinder and is based on a SS boundary condition. The natural frequencies of the analytical model (based on Love's equations), experimental natural frequencies, and frequencies predicted by FEA are shown in Table 2.2. The results are compared in Fig. 2.11.

It should be pointed out that in this work the cylinder's resonant frequency is used to approximate the location of the modal natural frequency. At a resonant frequency, the structural operating shape will be dominated by a particular mode at that frequency. Modal frequencies and resonant frequencies of a structure are not necessarily the same. This is especially true if the modes are not well separated. If adjacent modes are close in frequency, then the operating shape will be dominated by nearby modes. The operating shape has a contribution from all of the modes of a structure. Modes on the other hand are orthogonal and are essentially spatial basis functions that can be used in combination to describe the motion of the structure. The modal assurance criterion (MAC) is used in Appendix I to show the limitations of this approximation.

The analytical and FEA natural frequencies have an overall relative difference of 1.32% for the sixteen modes. The deviation between the analytical and experimental natural frequencies ranges from 0.5 to 24.5% depending on the mode. The major difference occurs in the two and three circumferential modes for the tested frequency range. It is believed that this deviation is caused because of the close proximity of the second (1200 Hz) and third (3850 Hz) modes of the

endplate. In general the analytical and experimental modes of the cylinder share the same modal order and are relatively close. The SS cylinder created to model an ideal SS cylinder is clearly not perfect. It does however have very similar vibrating properties and modal distribution. It should be pointed out that the cylinder is not perfectly uniform on its exterior surface. This is due to several other mounted PZT actuators and milled flats which were used for a previous experiment (Sumali, 1992). It is believed that these effects are minimal and should not significantly affect the vibrating properties of the cylinder.

2.5 Response to Various Actuator Locations

To help verify the response of the cylinder to excitation at different locations, the cylinder is excited at different positions and the response is compared (A: $x = 203.2$ mm, $\theta = 0^\circ$; B: $x = 135.5$ mm, $\theta = 0^\circ$; C: $x = 304.8$ mm, $\theta = 22.5^\circ$). Actuator A, B, and C are used to excite the cylinder at 25 Vrms using a sine-dwell test over a broad frequency range measured at $x =$ 338.7 mm $\theta = 0^\circ$ for actuator A and B and $x = 67.73$ mm, $\theta = 22.5^\circ$ for actuator C. The analytical and experimental results are shown in Figs. 2.12 and 2.13, respectively. For actuator A, the analytical model predicts the actuator will strongly excite the odd axial modes and ignore the even axial modes. This makes physical sense since actuator A is located at the center of the cylinder and is verified by Fig. 2.13. For actuator B, the analytical model predicts the actuator will excite the odd axial modes and will ignore the three axial modes. Similar trends are seen in Fig 2.13. Lastly, the actuator located ¼ of the length of the cylinder, actuator C, is predicted to excite the axial two modes the most. This is also confirmed by the experiment. An exception to this general behavior occurs at the (6,2) mode where it is expected that actuator A should not produce any excitation. However, both the analysis and experiment show a strong coupling at that frequency. The overall analytical response follows the expected physical trends with respect to actuator location and is similar to the experimental results.

2.6 Analytical and Experimental Response

Presented in Figs. 2.14 and 2.15 are the analytical and experimental response of the cylinder for actuator A and B measured at $x =$ 338.7 mm, $\theta = 0^\circ$. The relative magnitude of the predicted response is within half an order of magnitude compared to the measured response using an overall structural damping value of 0.5% (the predicted response magnitude depends on the damping value). Even though the frequencies of some modes are shifted, the dominant behavior of the cylinder is predicted by the model and the relative magnitudes are reasonably close.

For the analytical natural frequencies, which correspond to the (4,1) and (3,2) modes, the analytical spatial displacement response is shown in Figs. 2.16 and 2.17. The response of the cylinder has been unwrapped and so results can be more easily plotted. The phase of the displacement response has been incorporated into the plots to show actual normal displacements. As is expected for each of these frequencies, the predicted operating shape is similar to the dominant mode. The results indicate that the impedance model for PZT's actuating a SS cylinder can approximate the overall resonant and modal behavior.

Table 2.2 Cylinder analytical, FEA, and experimental natural frequencies

Mode	Analytical	FEA	Experimental
(3,1)	981 (Hz)	968	975
(2,1)	1084	1079	950
(4,1)	1530	1512	1538
(3,2)	2022	2000	1838
(4,2)	2082	2039	2044
(1,1)	2190	2189	2232
(5,1)	2378	2351	2395
(5,2)	2740	2679	2731
(2,2)	2798	2793	2113
(4,3)	3013	2950	2831
(3,3)	3251	3223	-
(5,3)	3420	3321	3337
(6,1)	3440	3397	3475
(6,2)	3739	3657	3760
(4,4)	4065	3983	3800
(2,3)	4153	4145	3363
(6,3)	4289	-	4233
(5,4)	4331	-	4168
(3,4)	4352	-	3925

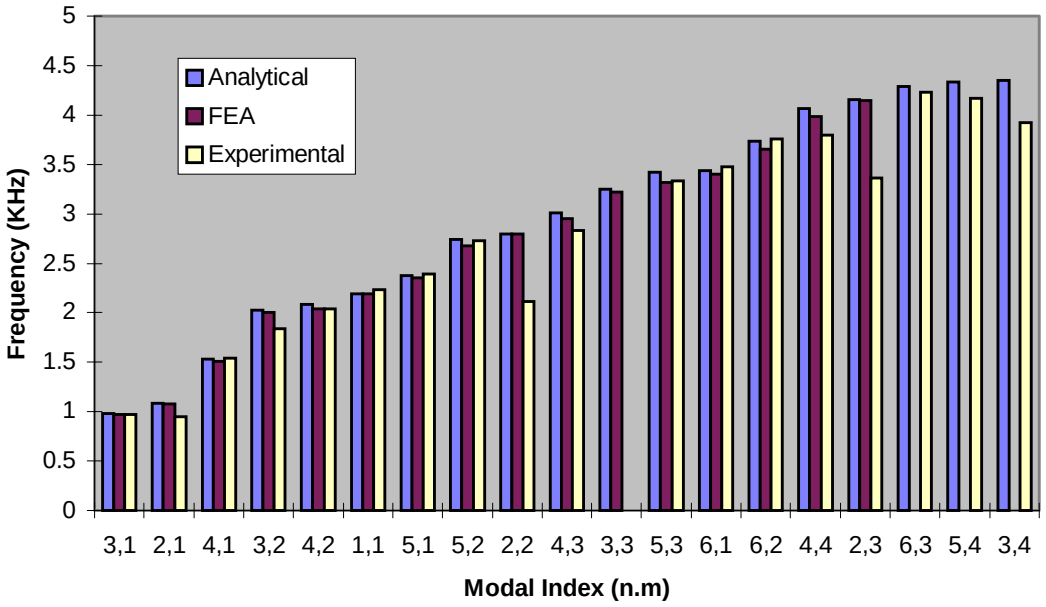

Figure 2.11 Comparison of analytical, FEA, and experimental natural frequencies.

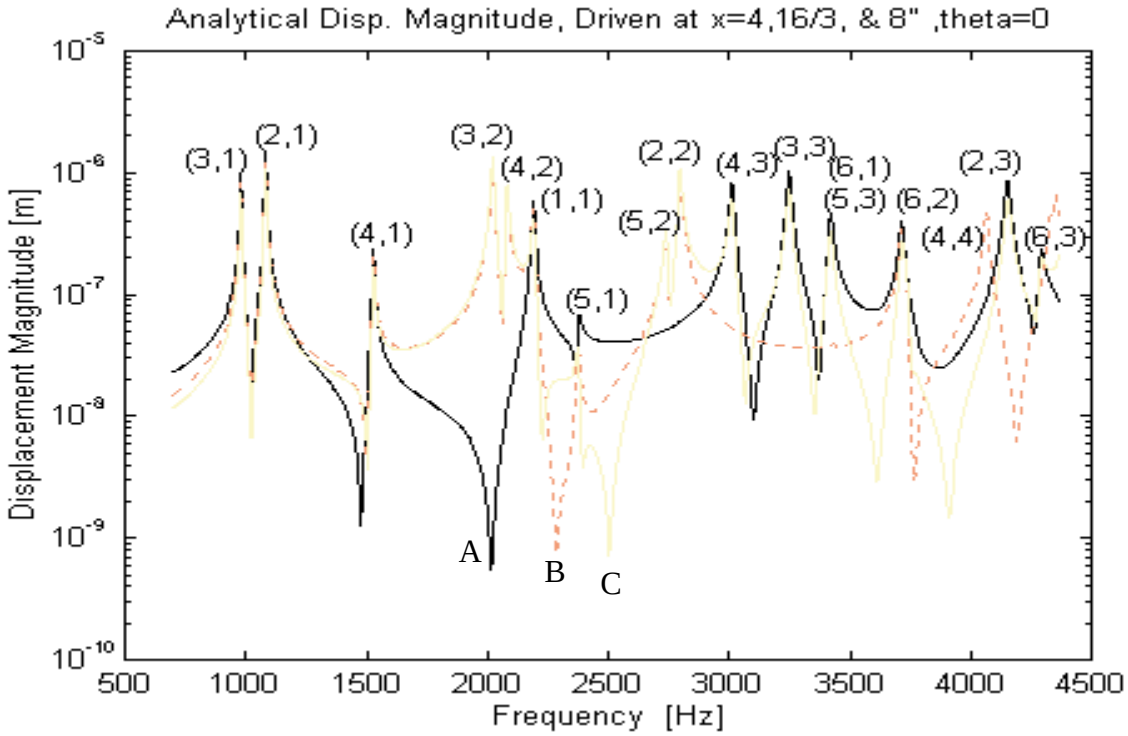

Figure 2.12 Analytical displacement magnitude driven by actuator A, B, and C.

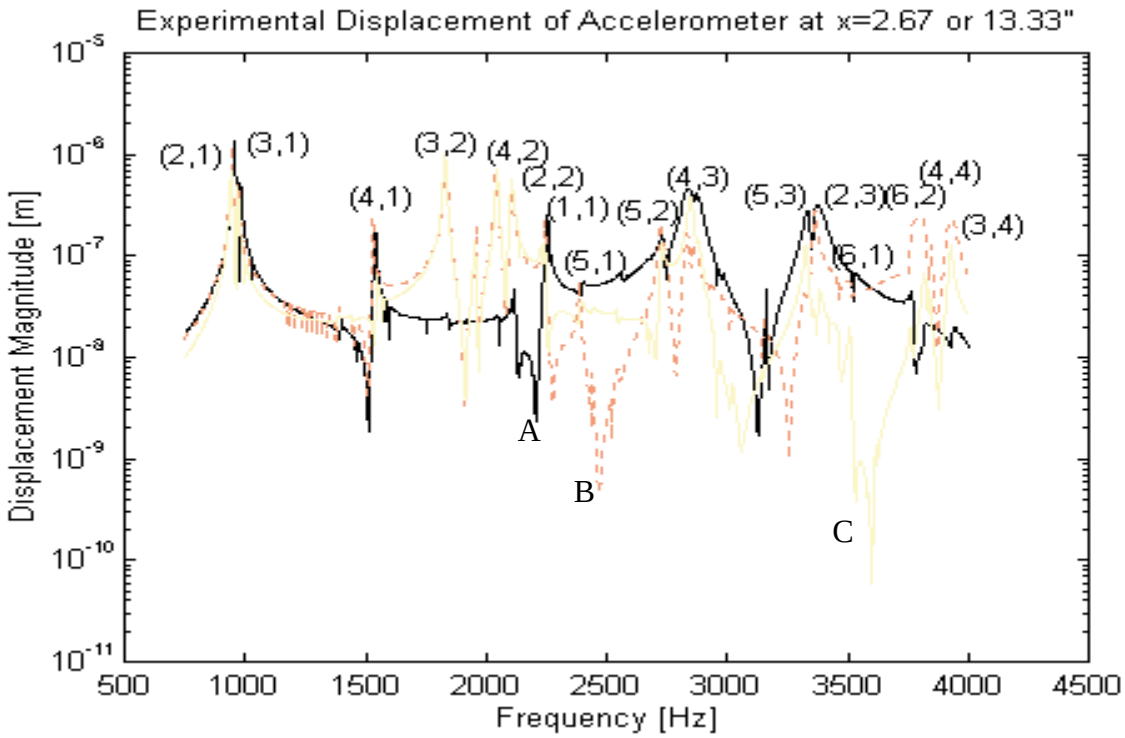

Figure 2.13 Experimental displacement magnitude driven by actuator A, B, and C.

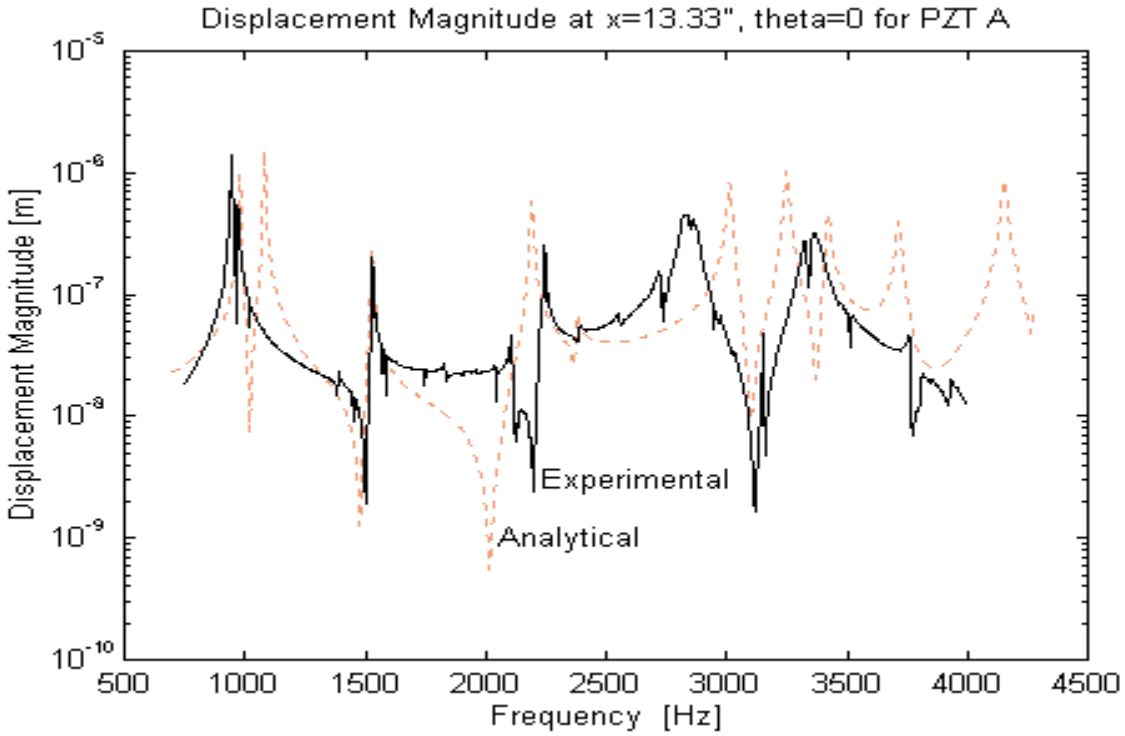

Figure 2.14 Analytical/experimental displacement magnitude for PZT A at 25 Vrms.

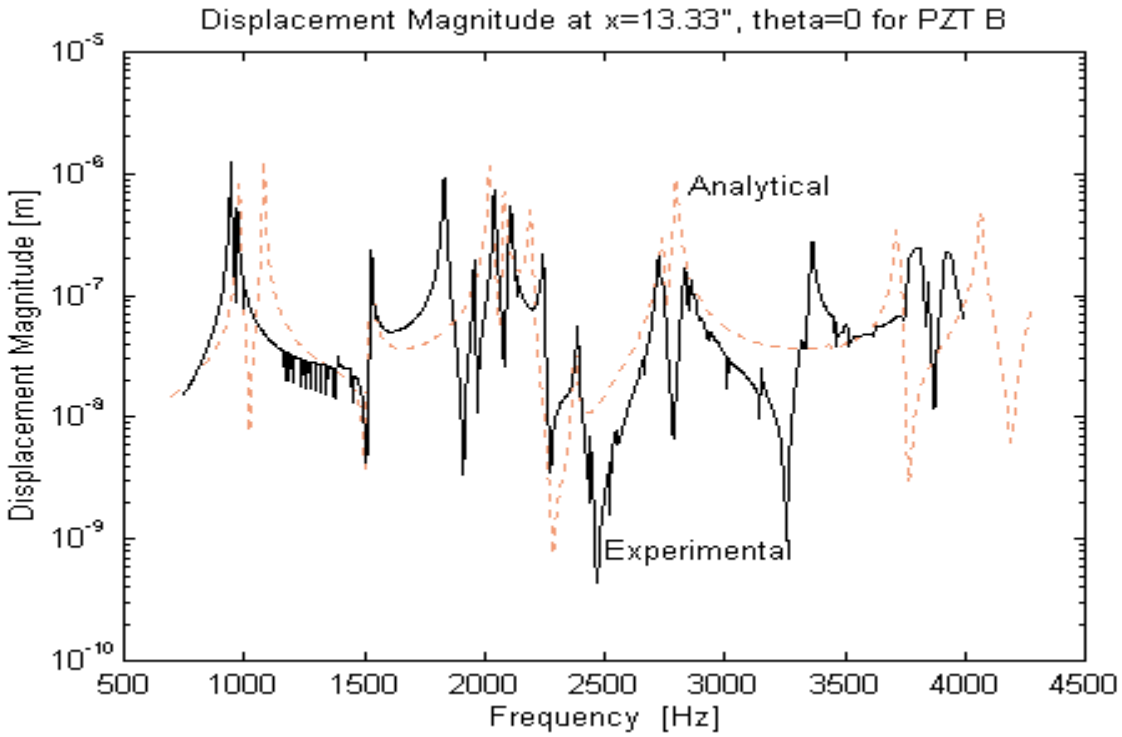

Figure 2.15 Analytical/experimental displacement magnitude for PZT B at 25 Vrms.

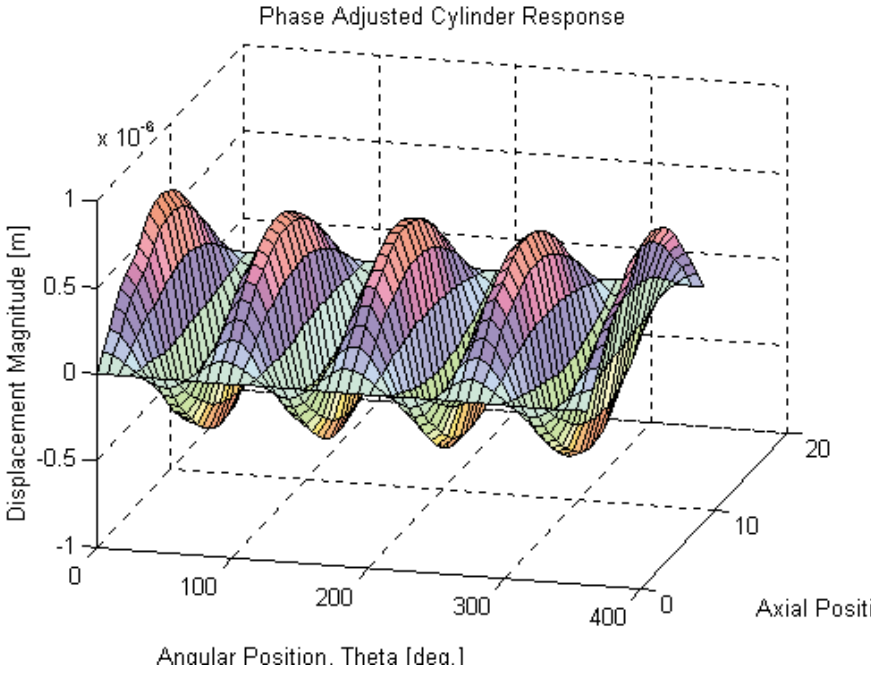

Figure 2.16 Analytical response at 1533 Hz (4,1).

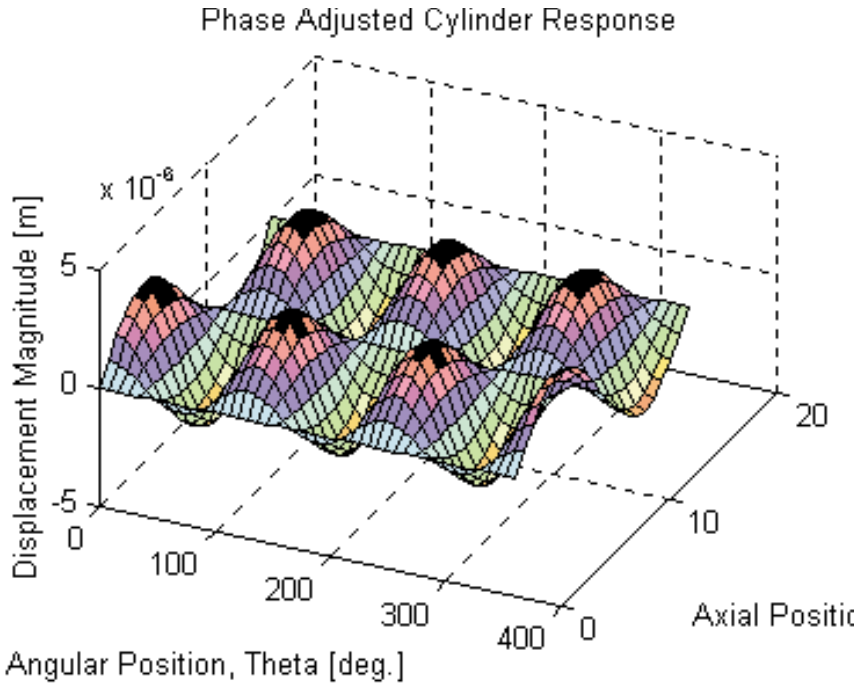

Figure 2.17 Analytical response at 2021 Hz (3,2).

2.7 Concluding Remarks on the Structural Model

In this chapter the structural response of a simply-supported (SS) cylinder excited by piezoelectric (PZT) actuators is presented. The theoretical formulation of Lalande's impedance model of a PZT actuator exciting a SS cylinder is reviewed. The creation of a SS boundary condition on an actual cylinder is also described along with the dynamic response of the cylinder. The results indicate that the relative magnitude of the predicted response is similar to the measured response for the cylinder tested. The model is able to predict the general modal behavior of the cylinder although the natural frequencies of some modes are shifted. These frequencies shifts are likely due to the interaction between the cylinder and the endplate's second and third modes. For a complex structure, like a cylinder, some inconsistent results can be expected. The analytical natural frequencies compared to those predicted by finite element analysis are in agreement. Also, the operating shape of the cylinder predicted by the model at a particular natural frequency is similar to the corresponding dominant mode shape. This is indicative that the model is valid. Even though the frequencies of some modes are shifted, the dominant behavior of the cylinder is predicted by the model and the relative displacement magnitudes are reasonably close (within half an order of magnitude). For the acoustic analysis performed in this work, the exact location of the resonant frequencies are not critical. The reason for this will be further described in later chapters. Since it is the magnitude and spatial displacement pattern of the operating shape that is more important to this overall analysis, the impedance model is acceptable. The model will be used to predict the structural response of a large scale cylinder which emulates a rocket payload fairing (PF).